ChemPubSoc Europe

DOI: 10.1002/cctc.201902066

CHEMCATCHEM Communications



# Development of Highly Stable Low Ni Content Catalyst for Dry Reforming of $CH_4$-Rich Feedstocks

Quan Luu Manh Ha,[a, b] Henrik Lund,[a] Carsten Kreyenschulte,[a] Stephan Bartling,[a] Hanan Atia,[a] Than Huyen Vuong,[a] Sebastian Wohlrab,[a] and Udo Armbruster*[a]

Highly active and coking-resistant Ni catalysts suited for the dry reforming of $CH_4$-rich gases (70 vol%, e.g. biogas or sour natural gas) were prepared starting from a Mg-rich Mg–Al hydrotalcite support precursor. Calcination at 1000 °C yields two phases, MgO and $MgAl_2O_4$ spinel. Complexation-deposition of Ni with citric acid on the preformed support as well as lanthanum addition yields a catalyst with remarkably low carbon accumulation over 100 h on stream attributed to both high Ni dispersion and preferred interactions of Ni with MgO on $MgAl_2O_4$.

Global energy demand is rapidly growing, and over 80% thereof is covered by fossil fuels in recent time.[1] Natural gas and biogas are emerging feedstocks for the energy market due to their abundance and low specific carbon footprint of the main component methane.[2–4] However, most natural gases and biogases contain varying amounts of other compounds.[5] For instance, some major natural gas sources in Vietnam[6] or biogases in Germany[7] contain a high fraction of $CO_2$ (~ 30 vol%). As separation is costly, dry reforming (DRM) is considered to directly convert such $CO_2$-rich gases into synthesis gas, a highly preferred starting material in large-scale chemical syntheses.[8] Mostly, DRM has been investigated with stoichiometric mixtures of $CH_4$ and $CO_2$. Processing feeds with an under-stoichiometric concentration of $CO_2$ via DRM may lead to higher $H_2$ fractions but encounters high coking rate due to the shortage in $CO_2$, which otherwise removes the surface carbon via gasification during the reaction.[9]

Nickel is the most commonly studied non-noble metal in DRM[9] because of its low cost and high availability.[5] However, Ni catalysts are prone to fast deactivation by coke deposition. Consequently, this issue was tackled via applying basic supports, adding dopants/modifiers, controlling the metal loading, or tuning preparation method and thermal pre-treatment.[5,10] Another serious problem is the aggregation of Ni species to larger but less active particles.

Several main steps rule the DRM reaction:[11] (1) Dissociative adsorption of $CH_4$ and $CO_2$, (2) first desorption of CO and $H_2$, (3) formation of surface hydroxyls and oxygen spill-over and (4) surface hydroxyls and oxygen oxidize $CH_x$ species and second desorption of CO and $H_2$. The adsorbed oxygen species from $CO_2$ dissociation react with carbonaceous intermediates (Table S. 1) which otherwise might form carbon. Consequently, we chose several approaches to enhance the activation of $CO_2$ at high Ni metal dispersion to suppress methane decomposition.

In our previous study on stoichiometric DRM ($CH_4/CO_2 = 1$), MgO–$Al_2O_3$ supported Ni catalyst modified with La and citric acid (CA) (denoted as La.Ni(CA)/$Mg_{1.3}AlO_x$) turned out to be most effective.[12] However, the coking behavior of this sample in $CH_4$-rich DRM is still unsatisfactory and limits process development. In this study, the thermal pre-treatment of the Mg-rich Mg–Al hydrotalcite support precursor was extended from 550 to 1000 °C. With this modification, the nature of the support was significantly changed as discrete oxide phases were formed, leading to improved interactions with the subsequently added Ni during DRM. The scheme of the preparation route is shown in Figure S. 1. For comparison, two catalysts were prepared on supports which were initially treated at 550 °C. Pathways for carbon formation were studied in order to understand the relationship between catalyst properties and coking resistance.

XRD pattern of the support $Mg_{1.3}AlO_x$.1000 (prepared by pre-treating $Mg_{1.3}AlO_x$ at 1000 °C) shows sharp reflections of periclase (the cubic form of MgO, ICDD file No. 01-071-1176)[13] and $MgAl_2O_4$ (ICDD file No. 00-021-1152)[14] crystalline phases (Figure 1a). The corresponding catalysts Ni/$Mg_{1.3}AlO_x$.1000 and La.Ni(CA)/$Mg_{1.3}AlO_x$.1000 display patterns close to that of the support, suggesting the formation of finely dispersed $La^{3+}$ and $Ni^{2+}$ species that are not detectable by XRD.[15] Moreover, magnification of the pattern for La.Ni(CA)/$Mg_{1.3}AlO_x$.1000 in the 2θ range from 61° to 64° exposes a slight shift of the reflection at 62.3° to higher 2θ values compared to support (Figure S. 2). This shift suggests the presence of NiO–MgO solid solution in La.Ni(CA)/$Mg_{1.3}AlO_x$.1000 formed from the Ni precursor and the preformed small MgO particles of 8–9 nm crystallite size.[16] In contrast, in $Mg_{1.3}AlO_x$ and corresponding catalysts the crystalline MgO (periclase) did not form. Instead, existence of

[a] Dr. Q. L. M. Ha, Dr. H. Lund, Dr. C. Kreyenschulte, Dr. S. Bartling, Dr. H. Atia, Dr. T. H. Vuong, Dr. S. Wohlrab, Dr. U. Armbruster
Leibniz Institute for Catalysis
Albert-Einstein-Str. 29a,
Rostock D-18059 Rostock (Germany)
E-mail: udo.armbruster@catalysis.de
[b] Dr. Q. L. M. Ha
Vietnam Petroleum Institute
167 Trung Kinh
Cau Giay 10000 (Vietnam)

Supporting information for this article is available on the WWW under https://doi.org/10.1002/cctc.201902066



 

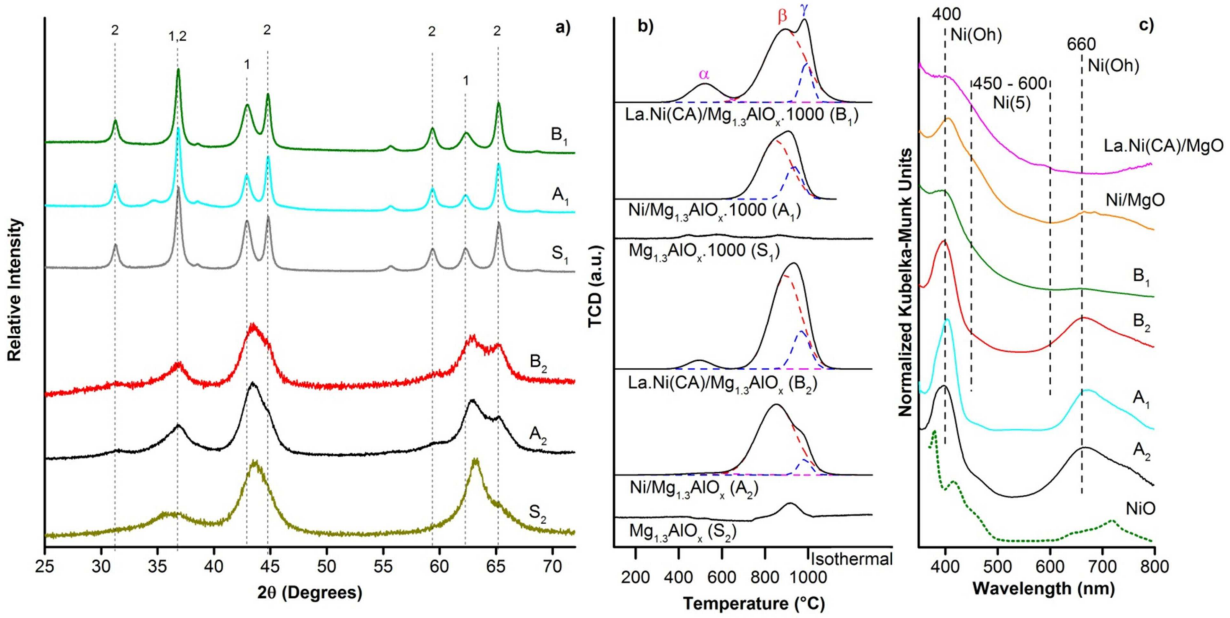


**Figure 1.** Structural characterization, reducibility and Ni coordination of $Mg_{1.3}AlO_x$.1000, $Mg_{1.3}AlO_x$ and their corresponding catalysts: a) XRD patterns, crystalline phases 1 = periclase (MgO), 2 = $MgAl_2O_4$; b) temperature-programmed reduction with $H_2$; c) UV-Vis-DR spectra in the region 350–800 nm of catalysts plus references NiO, Ni/MgO and La.Ni(CA)/MgO (Ni(Oh)=Ni in octahedral coordination; Ni(5)=Ni surface species in fivefold coordination).

$MgO–Al_2O_3$ solid solution is suggested which was previously discussed.[12]

Regarding the chemical surface states, the Ni $2p_{3/2}$ binding energy (Figure S. 3) from the XPS measurement of $Ni/Mg_{1.3}AlO_x$ (856.9 eV) indicates $Ni^{2+}$ located at the surface as $NiAl_2O_4$ spinel (856.8 eV).[17] The Ni $2p_{3/2}$ binding energy of $Ni/Mg_{1.3}AlO_x$.1000 (856.1 eV) is close to that of Ni surface species in NiO–MgO solutions (855.7–856.0 eV).[18–19] However, no Ni $2p_{3/2}$ signal was found in Ni/MgO with same Ni load, probably due to the migration of NiO into bulk MgO at high calcination temperature.[20] This confirms the unique structure of $Mg_{1.3}AlO_x$.1000, which can stabilize Ni in NiO–MgO solid solution but still offers surface Ni species that are beneficial for the catalytic activity.

Compared to pure NiO which can be significantly reduced at 400 °C,[12] all supported Ni samples display poorer reducibility in $H_2$-TPR experiments (Figure 1b) as the main reduction peaks appear first above 600 °C (β and γ peaks). This behavior is assumed to be caused by the strong metal-support interactions (MSI) at low Ni loading allowing $Ni^{2+}$ to disperse easily into stable structures.[21–22] $Ni/Mg_{1.3}AlO_x$.1000 discloses poorer overall reducibility compared to $Ni/Mg_{1.3}AlO_x$, illustrated by a higher percentage of $H_2$ uptake in γ peak (Table S. 2) and lower total $H_2$ consumption (Table 1).

$La.Ni(CA)/Mg_{1.3}AlO_x$.1000 consumes less $H_2$ in TPR than La.Ni $(CA)/Mg_{1.3}AlO_x$, but more than $Ni/Mg_{1.3}AlO_x$.1000 (Table 1) and even more than the theoretical value for complete $Ni^{2+}$ reduction (428 μmol). The latter can be traced back to enhanced oxygen activation from distorted Ni surface structures that will be discussed below in the UV-Vis section. Besides, it should be noted that CA-assisted preparation increases the $Ni^{2+}$ dispersion.[23] However, similar to $La.Ni(CA)/Mg_{1.3}AlO_x$, sample $La.Ni(CA)/Mg_{1.3}AlO_x$.1000 exposes a reduction peak below 600 °C (α peak) but with higher intensity (Figure 1b, Table S. 2). This effect is attributed to the presence of La that promotes the oxygen mobility and/or formation of defect structures where MgO is doped with $Ni^{2+}$.[12,24] On the other side,sample La.Ni $(CA)/Mg_{1.3}AlO_x$.1000 exposes the β peak at a temperature similar to that of $La.Ni(CA)/Mg_{1.3}AlO_x$ and an additional split γ peak at very high temperature (980 °C) assigned to Ni in strong interaction with the support .[25]

These β and γ $Ni^{2+}$ species are poorly reduced in usual pre-treatment and therefore $La.Ni(CA)/Mg_{1.3}AlO_x$.1000 is only partially reduced before DRM. The Ni metal fraction after *in situ* reduction was evaluated in a two-step experiment: first, the reduction at 700 °C was made, directly followed by a regular TPR experiment up to 1000 °C. This revealed a $H_2$ uptake of 292 μmol/g, corresponding to 59% of the value for the fresh

**Table 1.** Specific BET surface area, $H_2$ consumption from $H_2$-TPR data and La, Ni contents (ICP) of Ni catalysts and supports*.

| Sample | $A_{BET}$ [$m^2$/g] | $H_2$ uptake [μmol/g] | Metal content [wt%] Ni | La |
|---|---|---|---|---|
| $Mg_{1.3}AlO_x$ | 180 | 64 | – | – |
| $Ni/Mg_{1.3}AlO_x$ | 174 | 494 | 2.41 | |
| $La.Ni(CA)/Mg_{1.3}AlO_x$ | 144 | 521 | 2.49 | 4.54 |
| $Mg_{1.3}AlO_x$.1000 | 85 | 32 | – | – |
| $Ni/Mg_{1.3}AlO_x$.1000 | 82 | 404 | 2.40 | – |
| $La.Ni(CA)/Mg_{1.3}AlO_x$.1000 | 80 | 493 | 2.13 | 4.10 |

*Bare supports expose minor $H_2$ uptake, probably stemming from impurities.

catalyst at 700 °C. The rest is still $Ni^{2+}$ (Figure S. 4). This means that a large fraction of the Ni is in oxidised state after reduction.

Compared to support, Ni/$Mg_{1.3}AlO_x$ has similar BET surface area, whereas that of La.Ni(CA)/$Mg_{1.3}AlO_x$ is lower, probably caused by La addition (Table 1). The $Mg_{1.3}AlO_x$.1000 supported catalysts expose significantly lower values compared to $Mg_{1.3}AlO_x$-based materials, whereas La addition has no significant influence in this case.

The UV-Vis DR spectra in the region of 200–350 nm (Figure S. 5) give hints on the $Ni^{2+}$ ligand-to-metal charge transfer (LMCT) bands.[26] Ni/$Mg_{1.3}AlO_x$.1000 discloses a LMCT band with weaker intensity and blue shift compared to that of Ni/$Mg_{1.3}AlO_x$. This reflects a higher $Ni^{2+}$ dispersion, probably correlated with the stronger MSI of Ni/$Mg_{1.3}AlO_x$.1000.[27] Besides, modifying this material with La and CA-assisted synthesis shows further blue-shift of the UV band, indicating the formation of highly dispersed $Ni^{2+}$ in La.Ni(CA)/$Mg_{1.3}AlO_x$.1000.

The UV-Vis-DR spectra in the region 350–800 nm (Figures 1c and S. 6) reveal the coordination of $Ni^{2+}$.[15,17,28] The Ni catalysts expose mainly absorption bands at 400 nm and 660 nm, which are associated with $\nu_3$ ($^3A_{2g}\rightarrow{}^3T_{1g}$) and $\nu_2$ ($^3A_{2g}\rightarrow{}^3T_{1g}$) absorptions caused by $Ni^{2+}$ species in octahedral coordination (Oh), similarly to that of Ni/MgO spectra, instead of tetrahedral (Th) geometries. Such lack of $Ni^{2+}$ (Th) species reflects the presence of surplus MgO that stabilizes the $Ni^{2+}$ species and suppresses the formation of $NiAl_2O_4$ spinel.[29–31]

The XRD pattern of La.Ni(CA)/$Mg_{1.3}AlO_x$.1000 proves the presence of the periclase (MgO) structure, suggesting formation of NiO–MgO solid solution (Figures 1a and S. 2). Hence, the shoulder at 400–600 nm in the UV-Vis-DR spectrum recorded for La.Ni(CA)/$Mg_{1.3}AlO_x$.1000 suggests local defect structures in NiO–MgO solid solution[28] that can explain the α reduction peak at 400 °C (Figure 1b).[21,24,32] A similar shoulder is found in the UV-Vis spectra for Ni/MgO (Figure 1c) or La.Ni/$Mg_{1.3}AlO_x$.1000 (Figure S. 6) but with higher intensity/red shifts correlated to more $Ni^{2+}$ species in the local defect structures.

The UV-Vis spectrum of Ni/$Mg_{1.3}AlO_x$ shows two bands at 400 nm and 660 nm (Figure 1c), which were also found for La.Ni(CA)/$Mg_{1.3}AlO_x$ and Ni/$Mg_{1.3}AlO_x$.1000. However, La.Ni(CA)/$Mg_{1.3}AlO_x$.1000 reveals only a strong broad band at 400 nm ending at 600 nm, quite similar to that of La.Ni(CA)/MgO.

No Ni particles were observed in the representative STEM high-angle annular dark field (HAADF) image of fresh calcined La.Ni(CA)/$Mg_{1.3}AlO_x$.1000 (Figure S. 7). This result suggests, in accordance with the XRD patterns (Figure 1a) and UV-Vis-DRS data (Figure S. 5), that $Ni^{2+}$ species are highly dispersed in the structure of the support.[33] However, the EDX elemental maps and their corresponding HAADF image of this sample show the preferred location of Ni at Mg(La)-enriched regions with brighter contrast attributed to the high atom weight of La (Figure 2).

This was further validated by EDX spectra at regions 006 and 008, showing increased Ni concentration at Mg-/La-enriched locations (Figure S. 8). This preferred Ni location probably also proves the presence of NiO–MgO solid solution in La.Ni(CA)/$Mg_{1.3}AlO_x$.1000. As a result, finely dispersed $Ni^{2+}$ can

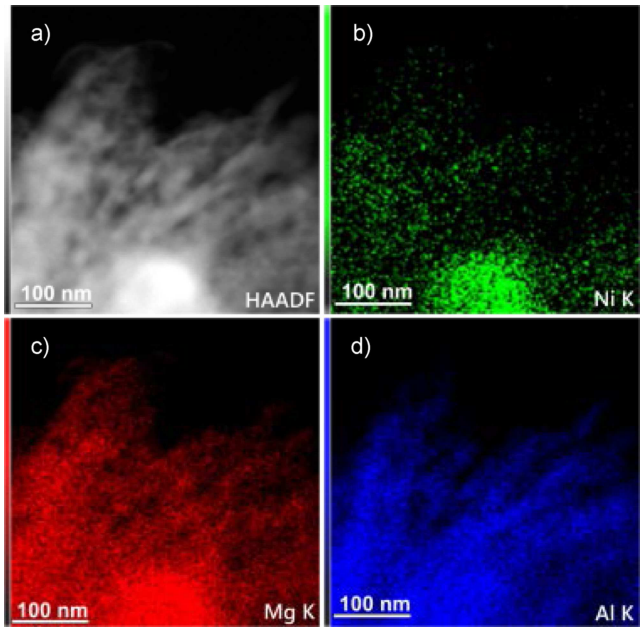


**Figure 2.** a) STEM-HAADF and EDX element mapping images of La.Ni(CA)/$Mg_{1.3}AlO_x$.1000 for b) Ni, c) Mg and d) Al.

only be partially reduced (Figure S. 4) and hardly aggregate to metallic Ni particles. However, good metal dispersion is achieved, and the particles are attached to the support (Figures S. 9b-2 and S. 10), mostly due to strong MSI of such $NiO_{1-x}$ and MgO in their solid solution.

The $CH_4$-rich DRM tests show that the thermal pre-treatment of the $Mg_{1.3}AlO_x$ support at 1000 °C remarkably improves the stability and coking resistance of the corresponding Ni catalysts in $CH_4$-rich DRM (Figures 3 and 4a). The measured conversions were below calculated equilibrium data (Figures S. 11 and S. 12). La.Ni(CA)/$Mg_{1.3}AlO_x$.1000 showed improved resistance against deactivation (Figure 3) and carbon accumulation (Figure 4a), which can be assigned to its reducibility (Figure 1b) and finely dispersed Ni atoms maintained during the reaction (Figures S. 9b-2, S. 9c-2, S. 13). In contrast, Ni agglomeration occurred with Ni/$Mg_{1.3}AlO_x$ already after the pre-reduction step and even more seriously during DRM (Figures S. 9b-1 and c-1) and led to bigger Ni particles that may cause serious deactivation and coking. The $H_2$/CO ratios reach unity, especially at 750 °C, reflecting a low contribution of reverse water gas shift reaction which otherwise would deteriorate the $H_2$ yield at high temperature with $CH_4$-rich feed (Figure S. 14).

At 750 °C, La.Ni(CA)/$Mg_{1.3}AlO_x$.1000, as the best catalyst among samples with this support (Figure S. 14a–c), performs similarly to La.Ni(CA)/$Mg_{1.3}AlO_x$. However, detected carbon amounts on spent samples of both catalysts after $CH_4$-rich DRM differ significantly from each other.

The coking pathways were studied in a series of runs with catalyst Ni/$Mg_{1.3}AlO_x$ at different temperatures (500–750 °C) using feeds composed of $CH_4$/Ar = 1 or 2 (both without $CO_2$) as well as $CH_4/CO_2 = 1$ or 2 at a GHSV of 170 L/($g_{cat}\times$h) (Figure 4b). The carbon deposits on spent samples were analyzed after 8 h on stream. At 500 °C, the carbon contents on all spent catalysts

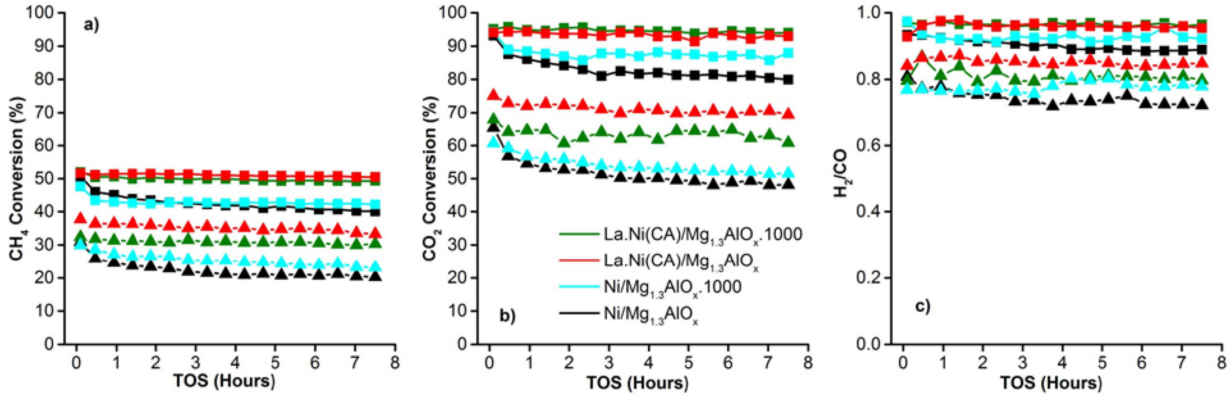


**Figure 3.** $CH_4$-rich DRM tests over Ni catalysts supported on $Mg_{1.3}AlO_x$ or $Mg_{1.3}AlO_x$.1000: a) $CH_4$ conversions, b) $CO_2$ conversions and c) $H_2$/CO ratio obtained at different temperatures (triangles = 630 °C; squares = 750 °C, 1 bar, $CH_4/CO_2 = 2$, GHSV = 170 L/($g_{cat}$ × h)). Catalysts were pre-reduced *in situ* at 700 °C for 1.5 h.

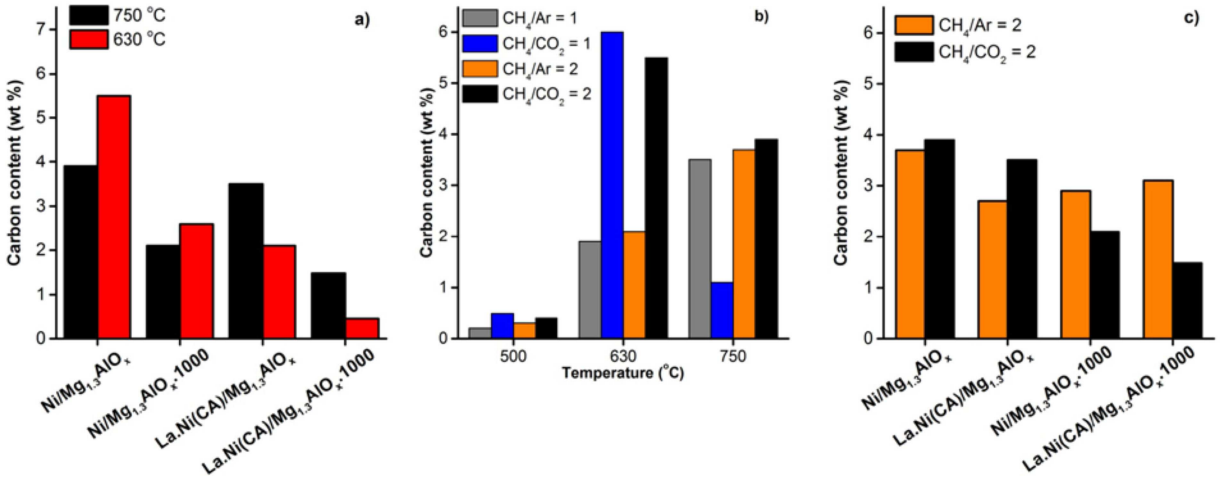


**Figure 4.** Fraction of carbon deposition on spent a) Ni catalysts after $CH_4$-rich DRM ($CH_4/CO_2 = 2$), b) $Ni/Mg_{1.3}AlO_x$ after tests with $CH_4/CO_2$ or $CH_4$/Ar at different temperatures and c) Ni catalysts after tests with $CH_4/CO_2$ or $CH_4$/Ar at 750 °C (1 bar, TOS = 8 h, GHSV = 170 L/($g_{cat}$ × h)).

were negligible, as methane decomposition (MD) and DRM (producing CO as a reactant for Boudouard reaction (BD)) run at higher temperatures. In all tests with $Ni/Mg_{1.3}AlO_x$ and $CH_4$/Ar, raising the temperature and $CH_4$ concentration caused a proportional rise in carbon deposition, reflecting the impact of methane decomposition and/or metal agglomeration.[34–35] When $CO_2$ was converted in DRM at 630 °C with $CH_4$ at any portion, the deposition was significantly higher, indicating the extent of BD reaction via CO disproportionation, which outnumbered MD contribution. However, at 750 °C, the contribution of BD decreased.[36] Indeed, when Ar is replaced by $CO_2$, the carbon deposition changes only slightly in case of $CH_4/CO_2 = 2$ but decreases dramatically at $CH_4/CO_2 = 1$ (higher $CO_2$ partial pressure), adapting to the thermodynamically favorable gasification (reversed BD) of C by $CO_2$ at high temperature.[34,37]

These data suggest that $La.Ni(CA)/Mg_{1.3}AlO_x$ has a structure modification effect that can slow down BD reaction, lowering the coking rate at 630 °C in $CH_4$-rich DRM (Figure 4a).[12] Nevertheless, at 750 °C carbon mainly formed by MD reaction is still observed on all spent $Mg_{1.3}AlO_x$-supported Ni catalysts due to the lower concentration of $CO_2$ and low efficiency in activation of $CO_2$. However, such carbon deposition can also be suppressed by applying $Mg_{1.3}AlO_x$.1000 supported Ni catalysts (Figure S. 15).

Further coking tests with $CH_4/Ar = 2$ (no $CO_2$) at 750 °C (Figure 4c) elucidate the specific influence of MD on carbon deposition. While $Mg_{1.3}AlO_x$ supported catalysts show similar or higher carbon contents after $CH_4$-rich DRM ($CH_4/CO_2 = 2$) than after MD ($CH_4/Ar = 2$), $Ni/Mg_{1.3}AlO_x$.1000 and especially $La.Ni(CA)/Mg_{1.3}AlO_x$.1000 form lower amounts of carbon in $CH_4$-rich DRM compared to MD. This contrast points to the high potential of the latter catalysts in $CO_2$ activation, even at low partial pressure, which cannot be achieved with Ni catalysts supported on $Mg_{1.3}AlO_x$. The $CO_2$ activation, in this case, reduced the coke deposition by MD reaction in $CH_4$-rich DRM by enhancing carbon gasification.

The clearly enhanced $CO_2$ activation by $La.Ni(CA)/Mg_{1.3}AlO_x$.1000 in $CH_4$-rich DRM might be attributed to the stronger influence of MgO on Ni finely dispersed in NiO–MgO solid solution than in $Ni/Mg_{1.3}AlO_x$ or La.Ni(CA)/

$Mg_{1.3}AlO_x$.[38–40] In the first step of the reaction, this structure is supposed to accelerate the $CO_2$ dissociation at the metal-support interface as well as the $CH_4$ cracking on Ni atoms,[41–42] thereby releasing the first CO and $H_2$ molecules.[11] With $La_2O_3$/$La_2O_2CO_3$ enriched around these metal atoms (Figure 2), defective sites (e.g. oxygen vacancies) are generated (Figure 1c), promoting dissociative $CO_2$ adsorption which subsequently forms surface oxygen species.[41,43–46] The increased availability of these oxygen species transforms carbonaceous intermediates from $CH_4$-rich mixture and releases second CO and $H_2$ (Table S. 1). This behavior enhances both the reaction rate and the carbon resistance of the catalyst even at low $CO_2$ partial pressure. Such solid solution was recently also supposed to be beneficial for $CH_4$-rich DRM by suppressing carbon formation.[47] However, concerning the loading of Ni and the catalyst productivity in that investigation (Table S. 3), the catalyst in the present study is superior. It should be noted that the mentioned NiO–MgO interaction is expected in Ni/MgO as well. However, due to low Ni loading, this sample showed almost no activity due to low Ni surface concentration.

La.Ni(CA)/$Mg_{1.3}AlO_x$.1000 was employed in a long-term test over 100 h at typical conditions to evaluate the application potential (Figure 5). In known literature,[9] a long-term $CH_4$-rich DRM run with such high feed rate was not reported.

Complete avoidance of carbon accumulation at high $CH_4$/$CO_2$ ratio with Ni catalysts was previously considered infeasible.[48] However, over 100 h of $CH_4$-rich DRM in the present study, the $H_2$/CO ratio remained constantly near unity whereas the conversions slightly decreased, but low carbon amount (~5 wt%) was found on the spent sample. This fraction was predictably higher than the values in DRM tests over 8 h, but not proportional to total run time. Interestingly, while carbon accumulation on spent La.Ni(CA)/$Mg_{1.3}AlO_x$.1000 was observed in STEM annular bright field (ABF) image after 8 h on stream, carbon was hardly found on the spent sample after 100 h (Figure S. 13), highlighting the exceptionally stable coking resistance due to gasification. This behavior is in accordance with the stable dispersion of small Ni particles (5–10 nm) which are also partially attached to the support (Figure S. 13). Besides, STEM-HAADF images prove that the mentioned preferred localization of Ni in the MgO-enriched structures is preserved during the reaction (Figures S. 16 and S. 17). These factors are crucial for both carbon removal by $CO_2$ and stably high DRM performance with high $H_2$ yield of La.Ni(CA)/$Mg_{1.3}AlO_x$.1000. In terms of active metal price and loading, productivity and stability against coking, La.Ni(CA)/$Mg_{1.3}AlO_x$.1000 is one of the most promising candidates for DRM under $CH_4$-rich conditions (Table S. 3).[47,49–51]

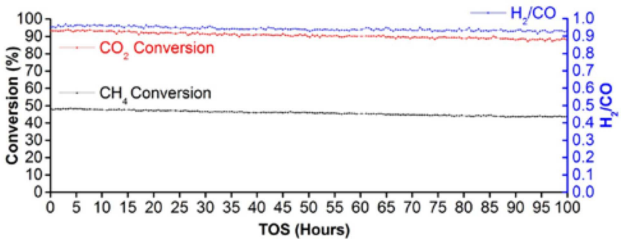


**Figure 5.** $CH_4$, $CO_2$ conversions and $H_2$/CO ratio in long-term $CH_4$-rich DRM with La.Ni(CA)/$Mg_{1.3}AlO_x$.1000 (750 °C, 1 bar, $CH_4/CO_2 = 2$, GHSV = 170 L/($g_{cat}$ × h)). Catalyst was pre-reduced *in situ* at 700 °C for 1.5 h.

We conclude that catalysts supported on $Mg_{1.3}AlO_x$.1000 possess improved coking resistance without losing the DRM activity and are therefore suitable for the reaction with $CH_4$-rich feed. Citric acid induces a high dispersion already during the catalyst preparation. The NiO–MgO solid solution domains excellently stabilize small Ni particles throughout all catalyst pre-treatment steps and DRM. Highly dispersed Ni activates $CO_2$ as an oxidant for carbon gasification, thereby reducing the coking rate in $CH_4$-rich DRM even at low $CO_2$ partial pressure. La generates additional oxygen vacancies that help to activate $CO_2$ as well. La.Ni(CA)/$Mg_{1.3}AlO_x$.1000 appears to be the best catalyst as it has high and stable activity over at least 8 h on stream and its coking rate is lowest at both 630 and 750 °C. Moreover, this catalyst exposes quite stable activity in $CH_4$-rich DRM over 100 h on stream with little coking. Such exceptional performance is certainly ruled by high Ni dispersion and enhanced reducibility.

## Experimental Section

Mg–Al mixed oxide supports were prepared from Mg–Al hydrotalcite (Pural MG50, Sasol). The default precursor $Mg_{1.3}AlO_x$ was obtained by calcining the Mg–Al hydrotalcite at 550 °C. This material was thermally pre-treated at 1000 °C with a rate of 2 K/min to prepare $Mg_{1.3}AlO_x$.1000 support.

In order to prepare the final catalysts, both supports were treated with $Ni(NO_3)_2 \cdot 6H_2O$ (99%, Alfa Aesar) and $La(NO_3)_3 \cdot 6H_2O$ (99%, ABCR GmbH) by wet impregnation (nominal Ni content 2.5 wt%). Citric acid (>99%, Alfa Aesar) was added simultaneously in some cases. The molar ratio of La and Ni was set to 0.8, and the CA/metal molar ratio was fixed at 1.5. The calculated amounts of Ni, La precursors and CA were dissolved in deionized water and the solution was stirred for 4 h at 50 °C. The Mg–Al supports were then added and the slurry was stirred at 60 °C for 15 h. Water was gradually removed by a rotary evaporator for 4 h and the samples were dried overnight at 120 °C and calcined at 400 °C for 3 h and then at 800 °C for 6 h both in air with a rate of 2 K/min. MgO (FLUKA) as well as its corresponding Ni-loaded samples La.Ni(CA)/MgO and Ni/MgO served as reference materials. Pure NiO was prepared by calcining $Ni(NO_3)_2 \cdot 6H_2O$ at 800 °C.

XRD powder patterns were recorded on a Panalytical X'Pert diffractometer equipped with a Xcelerator detector using automatic divergence slits and Cu K$\alpha$1/$\alpha$2 radiation (40 kV, 40 mA; $\lambda$ = 0.15406 nm, 0.154443 nm). Cu beta-radiation was excluded using a nickel filter foil. The samples were mounted on silicon zero background holders. The obtained intensities were converted from automatic to fixed divergence slits (0.25°) for further analysis. Peak positions and profile were fitted with Pseudo-Voigt function using the HighScore Plus software package (Panalytical). Phase identification was done by using the PDF-2 database of the International Center of Diffraction Data (ICDD).

The low-temperature $N_2$ adsorption was performed on a Micromeritics ASAP 2010 apparatus at −196 °C. The samples were degassed at 200 °C in vacuum for 4 h before the analysis.

The metal (Ni, Mg, Al, La) contents of the samples were determined by ICP-OES using a 715-ES device (Varian).

The carbon deposition on spent catalysts was analyzed using a TruSpec Micro CHNS analyzer (LECO Corporation). Up to 10 mg of the investigated sample were catalytically burned with oxygen in a helium stream at 1100 °C. The resulting gas was analyzed with an infrared detector and a thermal conductivity detector.

$H_2$-TPR experiments were performed with a Micromeritics Autochem II 2920 instrument with a thermal conductivity detector. A 300 mg sample was loaded into a U-shaped quartz reactor and heated in 5 %$O_2$/He (50 ml/min; r.t. to 400 °C with 20 K/min, 30 min hold, then cooled to r.t. in Ar flow). TPR run was made up to 1000 °C in 5 %$H_2$/Ar (50 ml/min; 10 K/min, final hold 30 min before cooling to r.t.). A TPR for pre-reduced sample was also conducted. After oxidation with 5 %$O_2$/He, the sample was pre-reduced in pure $H_2$ (50 mL/min) at 700 °C for 1.5 h to imitate the pretreatment in DRM setup. Then the system was cooled to r.t. and a regular TPR experiment was appended. The $H_2$ consumption peaks were recorded using a thermal conductivity detector.

XPS measurements were carried out with an ESCALAB 220iXL instrument (Thermo Fisher Scientific) with monochromatic Al Kα radiation (E = 1486.6 eV). Samples were prepared on a stainless-steel holder with conductive double sided adhesive carbon tape. The electron binding energies were obtained with charge compensation using a flood electron source and referenced to the C1s peak of adventitious carbon at 284.8 eV (C–C and C–H bonds). The peaks were deconvoluted with Gaussian-Lorentzian curves using the software Unifit.

UV-Vis-DR spectra were measured over 200–800 nm using a Cary 5000 spectrometer (Varian) equipped with a diffuse reflectance accessory (praying mantis, Harrick). $BaSO_4$ was used as a white reference standard and diluted material was used for the measurement with pure NiO because of its high Ni content.

STEM measurements were performed at 200 kV with an aberration-corrected JEM-ARM200F (JEOL, Corrector: CEOS). The microscope is equipped with a JED-2300 (JEOL) energy-dispersive X-ray-spectrometer (EDXS) for chemical analysis. The aberration-corrected STEM imaging (High-Angle Annular Dark Field (HAADF) and Annular Bright Field (ABF)) was performed under the following conditions: HAADF and ABF both were done with a spot size of approximately 0.13 nm, a convergence angle of 30–36° and collecting at semi-angles for HAADF and ABF of 90–170 mrad and 11–22 mrad, respectively. The sample was dry deposited without any pretreatment on a holey carbon film supported by a Cu-grid (300 mesh) and transferred to the microscope.

DRM tests were carried out with a fixed-bed continuous-flow quartz reactor (1 bar, GHSV = 170 L/($g_{cat}$ × h); 500–750 °C; 50 mg catalyst, grain size < 315 μm, diluted by 2 g of quartz). After *in situ* pre-reduction with pure $H_2$ (700 °C, 100 % $H_2$, 50 mL/min, 1.5 h), the temperature was adjusted and held for 8–100 h on stream. The feed was composed of 80 vol % $CH_4$ in He (pre-mixed, Air Liquide) and admixed pure $CO_2$ (Linde) to set $CH_4/CO_2 = 1$ or 2. Volumetric flow rates given in this study are related to 25 °C and 1 bar. He served as an internal standard for volume change determination during the reaction. Feed and product gases were analyzed by an on-line gas chromatograph (Agilent 6890) equipped with flame ionization detector (HP Plot Q capillary, 15 m × 0.53 mm × 40 μm) and thermal conductivity detector (Carboxene packed, 4.572 m × 3.175 mm) for analysis of hydrocarbons and permanent gases, respectively. Pure components were used as references for peak identification and calibration. Carbon balances were calculated from gas products reaching more than 97 %. Conversions and $H_2$/CO ratio were calculated from mole streams of fed and converted reactants.

## Acknowledgements

*This work was financially supported by German Academic Exchange Service (DAAD) in the "Research Grants – Doctoral Programs in Germany" (57129429). The authors would like to thank Mr. Reinhard Eckelt and Mrs. Anja Simmula for BET and ICP experiments, respectively.*

## Conflict of Interest

The authors declare no conflict of interest.

**Keywords:** dry reforming of methane · model biogas and natural gas · Ni catalyst · non-stoichiometric DRM · stability

[1] İ. Yıldız, in *Comprehensive Energy Systems* (Ed.: I. Dincer), Elsevier, Oxford, **2018**, pp. 521–567.
[2] S. Faramawy, T. Zaki, A. A. E. Sakr, *J. Nat. Gas Sci. Eng.* **2016**, *34*, 34–54.
[3] BP Statistical Review of World Energy; **2019**; https://www.bp.com/content/dam/bp/business-sites/en/global/corporate/pdfs/energy-economics/statistical-review/bp-stats-review-2019-full-report.pdf
[4] N. Abatzoglou, S. Boivin, *Biofuels Bioprod. Biorefin.* **2009**, *3*, 42–71.
[5] C. Papadopoulou, H. Matralis, X. Verykios, in *Catalysis for Alternative Energy Generation* (Eds.: L. Guczi, A. Erdôhelyi), Springer, New York, **2012**, pp. 57–127.
[6] F. Gerner; Vietnam: Maximizing finance for development (MFD) energy infrastructure assessment program; **2018**; https://auschamvn.org/wp-content/uploads/2018/05/1.-WB_March-2018-Vietnam-Energy-Sector-Assessment.pdf
[7] D. d. Graaf, R. Fendler; Biogas production in Germany; **2010**; http://www.spin-project.eu/downloads/0_Background_paper_biogas_Germany_en.pdf.
[8] M. C. J. Bradford, M. A. Vannice, *Catal. Rev. Sci. Eng.* **1999**, *41*, 1–42.
[9] A. N. Şener, M. E. Günay, A. Leba, R. Yıldırım, *Catal. Today* **2018**, *299*, 289–302.
[10] M. Usman, W. M. A. Wan Daud, H. F. Abbas, *Renewable Sustainable Energy Rev.* **2015**, *45*, 710–744.
[11] N. A. K. Aramouni, J. G. Touma, B. A. Tarboush, J. Zeaiter, M. N. Ahmad, *Renewable Sustainable Energy Rev.* **2018**, *82*, 2570–2585.
[12] Q. L. M. Ha, U. Armbruster, C. Kreyenschulte, H. Atia, H. Lund, H. T. Vuong, S. Wohlrab, *Catal. Today* **2019**, *334*, 203–214.
[13] P. Kim, C. J. Lee, *Catalysts* **2018**, *8*, 361.
[14] P. A. Kumar, M. P. Reddy, B. Hyun-Sook, H. H. Phil, *Catal. Lett.* **2009**, *131*, 85–97.
[15] S. Damyanova, B. Pawelec, K. Arishtirova, J. L. G. Fierro, *Int. J. Hydrogen Energy* **2012**, *37*, 15966–15975.
[16] M. Serra, P. Salagre, Y. Cesteros, F. Medina, J. E. Sueiras, *Phys. Chem. Chem. Phys.* **2004**, *6*, 858–864.
[17] C. Jiménez-González, Z. Boukha, B. de Rivas, J. R. González-Velasco, J. I. Gutiérrez-Ortiz, R. López-Fonseca, *Energy Fuels* **2014**, *28*, 7109–7121.
[18] A. Cimino, D. Gazzoli, V. Indovina, G. Moretti, M. Occhiuzzi, F. Pepe, *Top. Catal.* **1999**, *8*, 171–178.
[19] E. Ruckenstein, Y. Hang Hu, *Appl. Catal. A* **1999**, *183*, 85–92.
[20] F. Arena, A. Licciardello, A. Parmaliana, *Catal. Lett.* **1990**, *6*, 139–149.
[21] M. Jafarbegloo, A. Tarlani, A. W. Mesbah, J. Muzart, S. Sahebdelfar, *Catal. Lett.* **2016**, *146*, 238–248.
[22] C. Li, Y.-W. Chen, *Thermochim. Acta* **1995**, *256*, 457–465.
[23] Q. Zhang, K. Long, J. Wang, T. Zhang, Z. Song, Q. Lin, *Int. J. Hydrogen Energy* **2017**, *42*, 14103–14114.
[24] S. L. González-Cortés, I. Aray, S. M. A. Rodulfo-Baechler, C. A. Lugo, H. L. Del Castillo, A. Loaiza-Gil, F. E. Imbert, H. Figueroa, W. Pernía, A.

Rodríguez, O. Delgado, R. Casanova, J. Mendialdua, F. Rueda, *J. Mater. Sci.* **2007**, *42*, 6532–6540.
[25] Q. L. M. Ha, U. Armbruster, H. Atia, M. Schneider, H. Lund, G. Agostini, J. Radnik, H. T. Vuong, A. Martin, *Catalysts* **2017**, *7*, 157.
[26] B. Scheffer, J. J. Heijeinga, J. A. Moulijn, *J. Phys. Chem.* **1987**, *91*, 4752–4759.
[27] J. Escobar, J. Antonio De Los Reyes, T. Viveros, *Appl. Catal. A* **2003**, *253*, 151–163.
[28] A. Zecchina, G. Spoto, S. Coluccia, E. Guglielminotti, *J. Chem. Soc. Faraday Trans. 1* **1984**, *80*, 1875–1889.
[29] L. Zhang, Q. Zhang, Y. Liu, Y. Zhang, *Appl. Surf. Sci.* **2016**, *389*, 25–33.
[30] R. Zhang, G. Xia, M. Li, Y. Wu, H. Nie, D. Li, *J. Fuel Chem. Technol.* **2015**, *43*, 1359–1365.
[31] Z. Boukha, C. Jiménez-González, M. Gil-Calvo, B. de Rivas, J. R. González-Velasco, J. I. Gutiérrez-Ortiz, R. López-Fonseca, *Appl. Catal. B* **2016**, *199*, 372–383.
[32] A. Zecchina, G. Spoto, S. Coluccia, E. Guglielminotti, *J. Chem. Soc. Faraday Trans. 1* **1984**, *80*, 1891–1901.
[33] D. Li, R. Li, M. Lu, X. Lin, Y. Zhan, L. Jiang, *Appl. Catal. B* **2017**, *200*, 566–577.
[34] S. Wang, G. Q. Lu, G. J. Millar, *Energy Fuels* **1996**, *10*, 896–904.
[35] M. Argyle, C. Bartholomew, *Catalysts* **2015**, *5*, 145.
[36] M.-S. Fan, A. Z. Abdullah, S. Bhatia, *ChemCatChem* **2009**, *1*, 192–208.
[37] D. Pakhare, J. Spivey, *Chem. Soc. Rev.* **2014**, *43*, 7813–7837.
[38] E. Ruckenstein, Y. H. Hu, *Appl. Catal. A* **1995**, *133*, 149–161.
[39] S. Helveg, C. López-Cartes, J. Sehested, P. L. Hansen, B. S. Clausen, J. R. Rostrup-Nielsen, F. Abild-Pedersen, J. K. Nørskov, *Nature* **2004**, *427*, 426–429.
[40] H. S. Bengaard, J. K. Nørskov, J. Sehested, B. S. Clausen, L. P. Nielsen, A. M. Molenbroek, J. R. Rostrup-Nielsen, *J. Catal.* **2002**, *209*, 365–384.
[41] K. Tomishige, O. Yamazaki, Y. Chen, K. Yokoyama, X. Li, K. Fujimoto, *Catal. Today* **1998**, *45*, 35–39.
[42] M. García-Diéguez, C. Herrera, M. Á. Larrubia, L. J. Alemany, *Catal. Today* **2012**, *197*, 50–57.
[43] Z. Zhang, X. E. Verykios, S. M. MacDonald, S. Affrossman, *J. Phys. Chem.* **1996**, *100*, 744–754.
[44] X. E. Verykios, *Int. J. Hydrogen Energy* **2003**, *28*, 1045–1063.
[45] E. Ruckenstein, Y. H. Hu, *Catal. Lett.* **1998**, *51*, 183–185.
[46] P. M. Mortensen, I. Dybkjær, *Appl. Catal. A* **2015**, *495*, 141–151.
[47] M. Yu, K. Zhu, Z. Liu, H. Xiao, W. Deng, X. Zhou, *Appl. Catal. B* **2014**, *148–149*, 177–190.
[48] A. T. Ashcroft, A. K. Cheetham, M. L. H. Green, P. D. F. Vernon, *Nature* **1991**, *352*, 225.
[49] A. Horváth, G. Stefler, O. Geszti, A. Kienneman, A. Pietraszek, L. Guczi, *Catal. Today* **2011**, *169*, 102–111.
[50] J. Károlyi, M. Németh, C. Evangelisti, G. Sáfrán, Z. Schay, A. Horváth, F. Somodi, *J. Ind. Eng. Chem.* **2018**, *58*, 189–201.
[51] M. Németh, D. Srankó, J. Károlyi, F. Somodi, Z. Schay, G. Sáfrán, I. Sajó, A. Horváth, *Catal. Sci. Technol.* **2017**, *7*, 5386–5401.

Manuscript received: October 31, 2019
Revised manuscript received: December 13, 2019
Version of record online: January 27, 2020

 